FLASH Proton Radiotherapy Spares Normal Epithelial and Mesenchymal Tissues While Preserving Sarcoma Response

Anastasia Velalopoulou[1], Ilias V. Karagounis[1], Gwendolyn M. Cramer[1], Michele M. Kim[1], Giorgos Skoufos[2,3], Denisa Goia[1], Sarah Hagan[1], Ioannis I. Verginadis[1], Khayrullo Shoniyozov[1], June Chiango[4], Michelle Cerullo[4], Kelley Varner[4], Lutian Yao[5], Ling Qin[5], Artemis G. Hatzigeorgiou[2,3,6], Andy J. Minn[1], Mary Putt[7], Matthew Lanza[8], Charles-Antoine Assenmacher[8], Enrico Radaelli[8], Jennifer Huck[4], Eric Diffenderfer[1], Lei Dong[1], James Metz[1], Constantinos Koumenis[1], Keith A. Cengel[1], Amit Maity[1], and Theresa M. Busch[1]

ABSTRACT

In studies of electron and proton radiotherapy, ultrahigh dose rates of FLASH radiotherapy appear to produce fewer toxicities than standard dose rates while maintaining local tumor control. FLASH-proton radiotherapy (F-PRT) brings the spatial advantages of PRT to FLASH dose rates (>40 Gy/second), making it important to understand if and how F-PRT spares normal tissues while providing antitumor efficacy that is equivalent to standard-proton radiotherapy (S-PRT). Here we studied PRT damage to skin and mesenchymal tissues of muscle and bone and found that F-PRT of the C57BL/6 murine hind leg produced fewer severe toxicities leading to death or requiring euthanasia than S-PRT of the same dose. RNA-seq analyses of murine skin and bone revealed pathways upregulated by S-PRT yet unaltered by F-PRT, such as apoptosis signaling and keratinocyte differentiation in skin, as well as osteoclast differentiation and chondrocyte development in bone. Corroborating these findings, F-PRT reduced skin injury, stem cell depletion, and inflammation, mitigated late effects including lymphedema, and decreased histopathologically detected myofiber atrophy, bone resorption, hair follicle atrophy, and epidermal hyperplasia. F-PRT was equipotent to S-PRT in control of two murine sarcoma models, including at an orthotopic intramuscular site, thereby establishing its relevance to mesenchymal cancers. Finally, S-PRT produced greater increases in TGFβ1 in murine skin and the skin of canines enrolled in a phase I study of F-PRT versus S-PRT. Collectively, these data provide novel insights into F-PRT-mediated tissue sparing and support its ongoing investigation in applications that would benefit from this sparing of skin and mesenchymal tissues.

Significance: These findings will spur investigation of FLASH radiotherapy in sarcoma and additional cancers where mesenchymal tissues are at risk, including head and neck cancer, breast cancer, and pelvic malignancies.

[1]Department of Radiation Oncology, Perelman School of Medicine, University of Pennsylvania, Philadelphia, Pennsylvania. [2]Department of Electrical & Computer Engineering, University of Thessaly, Greece. [3]Hellenic Pasteur Institute, Athens, Greece. [4]Department of Clinical Studies and Advanced Medicine, School of Veterinary Medicine, University of Pennsylvania, Philadelphia, Pennsylvania. [5]Department of Orthopedic Surgery, Perelman School of Medicine, University of Pennsylvania, Philadelphia, Pennsylvania. [6]DIANA-Lab, Department of Computer Science and Biomedical Informatics, University of Thessaly, Greece. [7]Department of Biostatistics, Epidemiology & Informatics, Perelman School of Medicine, University of Pennsylvania, Philadelphia, Pennsylvania. [8]Department of Pathobiology, School of Veterinary Medicine, University of Pennsylvania, Philadelphia, Pennsylvania.

Note: Supplementary data for this article are available at Cancer Research Online (http://cancerres.aacrjournals.org/).

K.A. Cengel, A. Maity, and T.M. Busch contributed equally as a co-senior authors of this article.

Corresponding Author: Theresa M. Busch, Department of Radiation Oncology, University of Pennsylvania Smilow Center for Translational Research, Room 8-126, 3400 Civic Center Blvd, Bldg 421, Philadelphia, PA 19104-5156. E-mail: theresa.busch@pennmedicine.upenn.edu

Cancer Res 2021;81:4808–21

doi: 10.1158/0008-5472.CAN-21-1500

Introduction

Radiotherapy (RT) can be curative as a cancer treatment, but is also associated with acute and late toxicities. Hence, there is need for approaches to limit radiation-induced toxicity. FLASH RT, in which radiation is delivered at ultrahigh dose rates (>40 Gy/second), has been reported to produce fewer toxicities than standard RT without compromising local tumor control. Most FLASH studies have utilized electrons (1, 2), but proton FLASH RT provides deeper tissue penetration than electrons, as well as the favorable spatial characteristics of protons (much less penumbra than electrons and no exit dose in contrast to X-rays; refs. 3, 4). We recently published that, compared with standard dose rate, proton FLASH RT reduces long-term intestinal injury (5). In this report, we study the effects of FLASH proton RT on skin and the mesenchymal tissues of muscle and bone. Toxicities in these regions may be dose limiting in a variety of cancers.

High-dose radiation, often in combination with surgery, is used to treat cancers of the head and neck, breast, pelvic region, and sarcomas, commonly producing toxicities to skin, bone, and/or soft tissue (6). Skin toxicities acutely manifest as erythema, desquamation, and alopecia or skin atrophy, while fibrosis and ulcer formation develop as late effects (7). Other late effects of RT include osteoradionecrosis, fracture, impaired wound healing, and muscle atrophy, as well as lymphedema (8–10). Importantly, sarcoma is the archetypal mesenchymal cancer in which high dose RT is often used despite the high risk of toxicity. In an NCI Canada (NCIC) randomized trial for patients

with soft tissue sarcoma (STS) undergoing surgery with either pre-op or post-op radiation, ≥ grade 2 fibrosis was seen in 49% of patients, edema in 19%, and joint stiffness in 20% (11). Thus, injury to mesenchymal normal tissues remains a significant contributor to morbidity after radiation in the treatment of STS as well as many epithelial cancers.

FLASH RT reduces toxicities in animal models, including early demonstration in mouse lung that electron FLASH produced less fibrosis than the same dose delivered at standard (<1 Gy/second) dose rate (1). Sparing of other normal tissues by FLASH electron RT has also been demonstrated, including in brain (12, 13) and the gastrointestinal tract (GI; ref. 2). The mechanisms for sparing by FLASH are incompletely elucidated; dose-rate-dependent differences in hypoxia response/tissue microenvironment/redox chemistry (12, 14–17), stem cell proliferation (5, 18), and inflammatory signaling (1, 18–20) have been implicated in early studies.

F-PRT provides equivalent control of epithelial-derived cancers in murine models compared with standard proton RT (S-PRT), including pancreatic adenocarcinomas and head and neck squamous cell carcinomas (5, 19), but its effect on mesenchymal cancers has not been determined. In the current studies, we demonstrate equivalent F-PRT control of murine sarcomas compared with S-PRT, accompanied by less damage to relevant normal tissues including skin, lymphatics, bone, and muscle. Studies are informed by RNA-seq analyses that identify differential activation of specific gene pathways by F-PRT versus S-PRT. Finally, work is extended into tissues from an ongoing canine trial of F-PRT at our institution. Our studies clearly show reduction in mesenchymal tissue injury following F-PRT and indicate differential activation of specific gene pathways that generate mechanistic hypotheses for these effects.

Materials and Methods

Mice

Eight- to 10-week-old female C57BL/6 and C3H/HeJ mice (The Jackson Laboratory) were maintained in Association for Assessment and Accreditation of Laboratory Animal Care–accredited facilities and all procedures approved by the Institutional Animal Care and Use Committee (IACUC) at the University of Pennsylvania. To propagate fibrosarcoma syngeneic tumors, 5×10^5 cells from a sarcoma line established from the *LSL-Kras*$^{G12D/wt}$;*p53*$^{FL/FL}$ genetically engineered mouse model (GEMM) model (C57BL/6 background) at the fifth passage or 3×10^5 cells of the established RIF mouse sarcoma cell line (C3H/HeJ background, RRID:IMSR_JAX:000659) at the nineth passage were injected subcutaneously or intramuscularly in the right thigh. Cells from the *LSL-Kras*$^{G12D/wt}$;*p53*$^{FL/FL}$ GEMM model were recently isolated for the purpose of this research. The established RIF cell line has been maintained in the laboratory of Dr. Busch for more

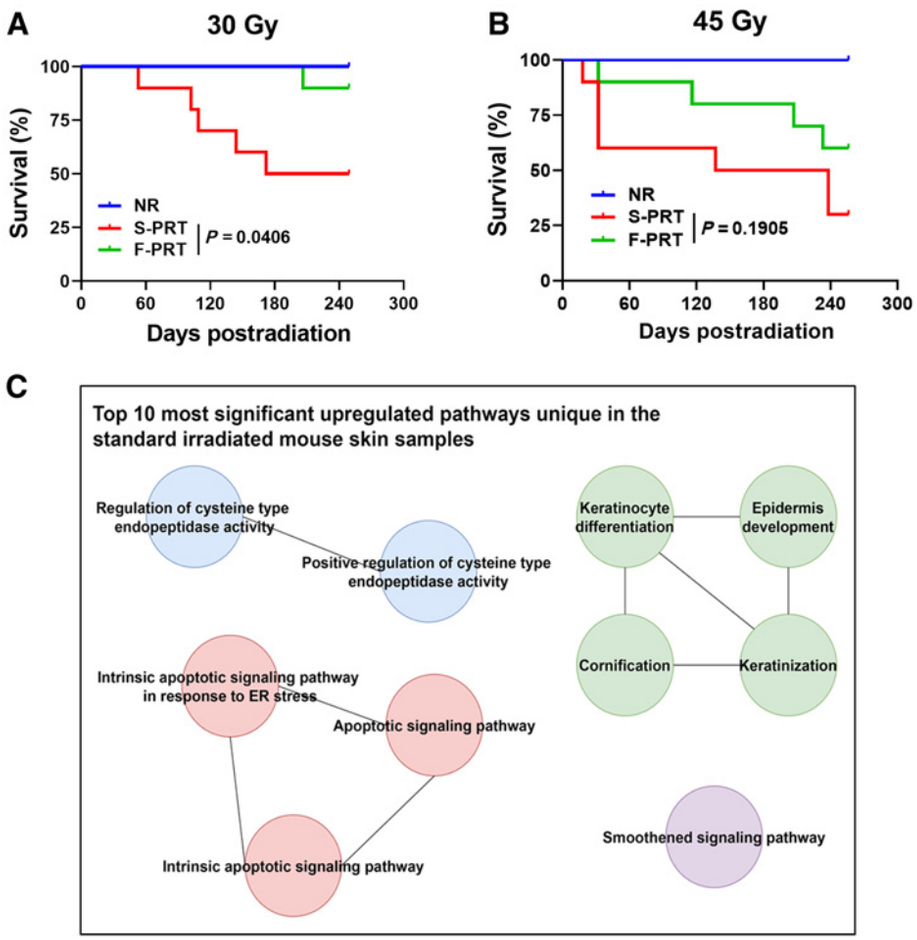

Figure 1.
F-PRT protects from morbidities and attenuates upregulation of pathways involved in keratinization and apoptosis, compared with S-PRT. **A** and **B,** Kaplan–Meier plots of survival following 30 Gy (**A**) and 45 Gy (**B**) of proton radiation, delivered to the mouse hind leg; $n = 10$, statistical analysis by log-rank test. Events record mortality or mandated euthanasia due to morbidity. **C,** Gene ontology enrichment analysis of the differentially expressed genes (upregulated) in the skin of S-PRT-treated mice compared with F-PRT-treated mice; $n = 4$ per group.

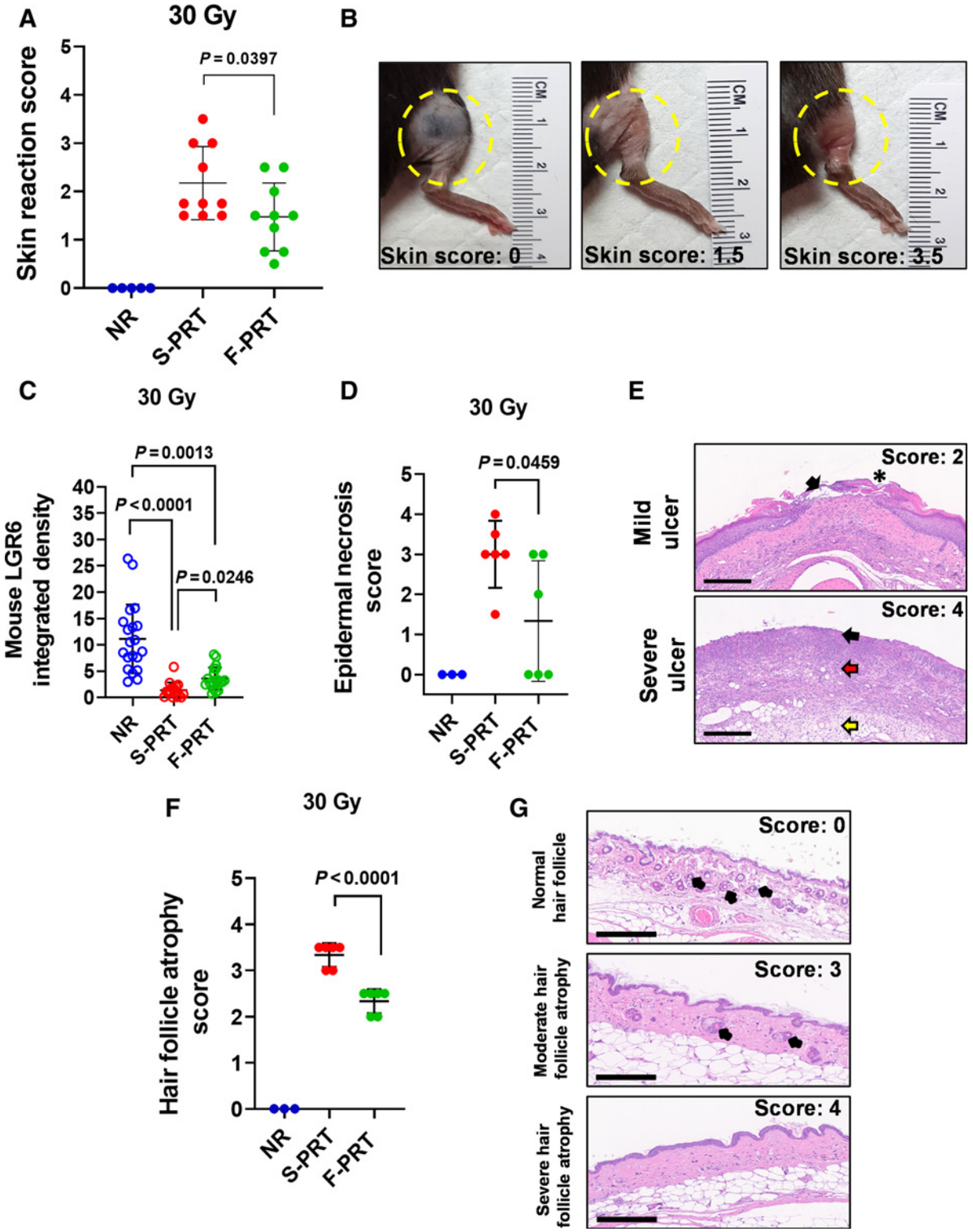

Figure 2.

F-PRT alleviates skin damage compared with S-PRT. **A,** Skin reaction of the irradiated leg after exposure to 30 Gy of F-PRT or S-PRT. Maximum skin score for each mouse is presented over an observation period of 8 months. NR, $n = 5$; F-PRT and S-PRT, $n = 10$; statistical analysis by Welch t test. **B,** Pictures of irradiated skin damage scored as 1.5 or 3.5 compared with untreated skin (score 0); score of 1.5 indicates localized breakdown of the skin with a scaly/crusty appearance, whereas 3.5 corresponds to full-thickness skin barrier loss. (*Continued on the following page.*)

than 20 years and originated from cells of the same line at Roswell Park Cancer Institute in Buffalo, NY. Both cell lines were authenticated and tested *Mycoplasma* negative by IDEXX BioAnalytics (CellCheck 19 plus) in 2021. Tumors were irradiated upon reaching 100 mm^3 in volume. Tumor size was measured utilizing calipers and volume was calculated as (length × $width^2$)/2.

Proton irradiation

Murine irradiation with FLASH (69–124 Gy/seconds) and standard (0.39–0.65 Gy/second) dose rates was carried out using a proton beam with energy 230 MeV (range ∼32 g/cm^2), delivered via a horizontal beam line in a dedicated research room with an IBA Proteus Plus (Louvain-La-Neuve) C230 Cyclotron. Mice were irradiated with the entrance (plateau) region of the beam with a field size of 2 cm × 2 cm (square collimator) per mouse for normal tissue studies and a 1-cm-diameter circular collimator for tumor studies. A double-scattered system was used to create a uniform field at the target with additional details on the irradiation set-up and dosimetry in the Supplementary Materials and Methods. Total dose (without any weighting for relative biological effectiveness) is as described for each study.

RNA sequencing

Briefly, raw RNA-seq datasets were quality checked and preprocessed, then alignment, gene-level quantification, and differential expression analysis were conducted using STAR (STAR, RRID: SCR_004463; ref. 21), RSEM (22), and EBSeq (23), respectively. This was followed by pathway enrichment analysis with details provided in the Supplementary Materials and Methods. RNA-seq datasets can be obtained under accession number GSE173944 in the gene expression omnibus database at NCBI.

Skin reaction and lymphedema scoring

Skin reaction was recorded using a published system of 10 grades, ranging from 0.5 to 3.5 (24). Lymphedema was scored as a function of its associated swelling using a system of four grades ranging from 0 to 4. Each grade represented the additional thickness in millimeters of swelling for the irradiated versus the nonirradiated foot.

Bioluminescence imaging of inflammation

Bioluminescence imaging of myeloperoxidase (MPO) activity is based on the systemic administration of luminol, allowing the quantification of phagocyte-mediated inflammation in the context of acute dermatitis (25). As described elsewhere (26), mice were intraperitoneally injected with luminol (300 mg/kg; luminol sodium salt, Sigma A465–5G) at indicated days postradiation. Bioluminescent images were acquired on an IVIS Spectrum imager (Perkin Elmer) from anesthetized (isoflurane) mice at 10 minutes after luminol injection when chemiluminescence signal reached maximum values, using a 5-minute exposure. Equally-sized regions of interest (ROI) were drawn around the irradiated area of the right hind leg of each mouse and the average radiance (photons/second/cm^2/sr) was quantified using Living Image Software 4 7.3 (Perkin Elmer).

Histopathology

Histopathology of skin and bone tissue was performed following standard protocol (described in Supplementary Materials and Methods) of the Comparative Pathology Core at the University of Pennsylvania School of Veterinary Medicine.

Fluorescence microscopy and image analysis

Fluorescence microscopy of 10 μm skin sections was performed to assess apoptosis by the TUNEL assay and Lgr6 and TGFβ1 expression by immunofluorescence. Quantification of immunofluorescence is presented as integrated density normalized to total nuclei area. Details on the staining process and image analysis are available in Supplementary Materials and Methods.

Canine sample collection

A trial of F-PRT versus S-PRT for dogs with clinical/radiographic diagnosis of extremity osteosarcoma was conducted with the approval of the IACUC at the University of Pennsylvania and the Privately Owned Animal Protocol committee and in collaboration with the Penn Veterinary Clinical Investigations Center at the University of Pennsylvania School of Veterinary Medicine. Dogs were randomly assigned to F-PRT versus S-PRT, delivered under general anesthesia to separate 2.6-cm-diameter circular areas of tumor-containing bone and normal bone. Five days following therapy, standard of care whole limb amputation surgery was performed and samples of irradiated and unirradiated tissues were collected in 10% buffered formalin for immunohistochemical analysis, as well as snap frozen for protein analysis. Details are provided in the Supplementary Materials and Methods.

Elisa

Mouse and dog skin sections (∼20 mg) were lysed in 1× RIPA containing protease and phosphatase inhibitors followed by homogenization and sonication. Samples (in duplicate) were quantified using the Pierce BCA Protein Assay (23225). Total TGFβ1 quantification was performed using the R&D Systems Mouse/Rat/Porcine/Canine TGFβ1 Quantikine ELISA Kit (MB100B). Forty microliters of each sample was assayed in duplicate after activation (1 N HCl), neutralization (1.2 N NaOH/0.5 M HEPES), and dilution with 50 μL of calibrator diluent. TGFβ1 levels were normalized by protein content.

Chromogenic immunohistochemistry

For immunohistochemistry (IHC), 5-μm-thick paraffin sections were mounted on ProbeOn slides (Thermo Fisher Scientific). The immunostaining procedure was performed using a Leica BOND RXm automated platform combined with the Bond Polymer Refine

(*Continued.*) **C,** Quantification of immunofluorescent detection of skin populations of $Lgr6^+$ stem cells at 18 days following 30 Gy of F-PRT versus S-PRT. $Lgr6^+$ cells were quantified on three to four skin sections per mouse ($n = 5$ mice, statistical analysis by Kruskal–Wallis test followed by Wilcoxon rank sum test.) **D,** Blinded evaluation of epidermal necrosis in skin hematoxylin and eosin–stained slides, at 27 days after 30 Gy of proton RT. NR, $n = 3$; F-PRT and S-PRT, $n = 5$; statistical analysis by Welch *t* test. **E,** Representative hematoxylin and eosin images of mild and severe ulceration. On the mild ulcer, black arrow points to ulcerated epidermis and an asterisk indicates a crust. On the severe ulcer, necrosis and inflammation are shown in the epidermis (black arrow), which extends through the dermis (red arrow) and subcutis (yellow arrow). Magnification, ×100. Scale bar, 300 μm. **F,** Blinded evaluation of hair follicle atrophy in skin hematoxylin and eosin–stained slides at 27 days after 30 Gy of PRT. NR, $n = 3$; S-PRT and F-PRT, $n = 6$. Statistical analysis by Welch *t* test. **G,** Representative images of hematoxylin and eosin–stained nonirradiated normal hair follicles and hair follicle atrophy of irradiated skin. Top, normal (nonirradiated) skin with normal hair follicle units (black arrows); middle, irradiated skin with hair follicle units (black arrows) that are reduced in number and size; bottom, hair follicles are completely absent. Hematoxylin and eosin, ×200 magnification. Scale bar, 200 μm. Values in **A**, **C**, **D**, and **F** represent mean ± SD.

Detection Kit (Leica, #DS9800). Staining and analysis of TGFβ1 was performed as described in the Supplementary Materials and Methods, on slides that were counterstained in hematoxylin.

Statistical analysis

Data are summarized using means, with SD as error bars unless otherwise noted. Parametric (ANOVA/*t* tests) or rank-based tests (Kruskal–Wallis/rank-sum) were chosen based on graphical inspection of the data. Multiple comparisons used either a Holm-Sidak approach (*t* tests) or a Dunn approach (rank-based tests) to achieve the family-wise type I error rate of 0.05. When the control lacked variation in an outcome, we compared only the F-PRT and S-PRT groups. All data are plotted and were analyzed in GraphPad Prism (version 8) or R (Version 3.6.1; GraphPad Prism, RRID:SCR_002798]; details appear in Supplementary Materials and Methods.

Results

F-PRT reduces severe morbidity compared with S-PRT

First, the sparing effect of F-PRT versus S-PRT was comprehensively investigated through survival studies, conducted following RT delivery to the murine hind leg with its associated tissues of skin, muscle and bone. At 30 Gy exposure (**Fig. 1A**), F-PRT provided significant protection from mortality or severe morbidity (mandating euthanasia) compared with S-PRT over the ∼250 days after irradiation. Morbidities included severe skin damage and soft tissue reaction assessed by ULAR veterinarians blinded to study groups. Median survival was 211 days after 30 Gy of S-PRT compared with >249 days for F-PRT ($P = 0.0406$). Increasing the RT dose to 45 Gy (**Fig. 1B**) decreased S-PRT median survival to 188 days, whereas the median survival exceeded 256 days for F-PRT. Notwithstanding, 60% of F-PRT animals did not succumb to severe morbidity within 256 days of 45 Gy treatment, a value statistically indistinguishable ($P = 0.1905$) from the 30% of animals that survived S-PRT at this dose. Collectively, these data show that F-PRT caused fewer severe morbidities leading to death or requiring euthanasia than S-PRT in normal tissues of the murine leg, with a dose of 30 Gy achieving statistical significance.

Transcriptome analysis of skin reveals pathways upregulated by S-PRT, yet unaltered by F-PRT

RNA-seq allowed insight into biological determinants of the differential effect of F-PRT versus S-PRT on murine skin. Full-thickness skin was collected 5 days after 30 Gy of F-PRT or S-PRT to the right hind leg to study transcriptome-level responses that could contribute to the survival-limiting morbidity presented above. We focused on this intermediate time point so as to capture gene expression changes that occurred early as a result of differences between the F-PRT and S-PRT modalities, as well as the potentially further effects driven by each modality. The top 10 pathways upregulated by S-PRT and unaltered by F-PRT were identified (**Fig. 1C**, with the involved genes provided in Supplementary Table S1). Pathways uniquely upregulated by S-PRT in murine skin included several associated with apoptosis and apoptotic signaling. Moreover, strong upregulation of pathways associated with keratin signaling, such as keratinocyte differentiation and cornification were uniquely identified in S-PRT versus F-PRT-treated skin.

We focused on genes and pathways upregulated by S-PRT and unaltered by F-PRT because of an interest in the types and mechanisms of tissue damage introduced by S-PRT while correspondingly spared by FLASH. However, some pathways were upregulated by F-PRT and unchanged by S-PRT (Supplementary Fig. S1A); for example, F-PRT, but not S-PRT, promoted upregulation of pathways related to tissue and vascular repair in the skin, including anatomical structure morphogenesis, blood vessel morphogenesis, and vascular development. These data suggest that F-PRT sparing of skin may result from less radiation-induced damage together with stronger expression of mechanisms for tissue repair. Other transcriptome-level differential effects of F-PRT versus S-PRT include pathways uniquely downregulated by each PRT modality (Supplementary Figs. S1B and S1C).

F-PRT spares skin from radiation-induced damage

Skin damage was a major driver of PRT-induced severe morbidity necessitating euthanasia (see **Fig. 1A** and **B**); moreover, RNA-seq of skin identified S-PRT to significantly upregulate apoptotic pathways that were unchanged by F-PRT. We evaluated PRT-induced skin damage based on a published scoring system (24), which assesses symptoms including erythema, dry/moist desquamation and partial/complete skin breakdown with loss of limb function. Skin reaction to PRT developed acutely (within weeks of irradiation), and mice treated with 30 Gy S-PRT to the hind leg developed a maximum skin reaction that was significantly ($P = 0.0397$) more severe than that those treated with F-PRT (**Fig. 2A** and **B**). Notably, the only mouse with a skin damage score of 3.5, indicating complete epidermal breakdown, was in the S-PRT-treated group.

In further interrogation of skin response, sections of treated skin were evaluated by immunofluorescent staining for stem cell markers. At both dose rates, PRT decreased the population of cells positive for $Lgr6^+$, a marker of skin stem cells (**Fig 2C**; Supplementary Fig. S2), which is consistent with the damaging effect of radiation. However, S-PRT produced greater $Lgr6^+$ cell depletion than F-PRT ($P = 0.0246$). Thus, these data suggest a mechanism by which the benefit of F-PRT could be propagated, that is, due to a comparatively higher number of stem cells available after F-PRT to promote epidermal regeneration in comparison with S-PRT.

Finally, the pathology of F-PRT sparing relative to S-PRT was histologically evaluated in skin sections. Histopathology showed F-PRT to reduce the extent of epidermal necrosis compared with S-PRT ($P = 0.0459$; **Fig. 2D** and **E**). The increased presence of unhealed skin lesions after S-PRT versus F-PRT is consistent with both RNA-seq evidence of greater induction of apoptosis after S-PRT and the significantly greater depletion of skin stem cells by this dose rate. Interestingly, F-PRT also significantly reduced hair follicle atrophy compared with S-PRT at 27 days after PRT ($P < 0.0001$; **Fig. 2F** and **G**). This atrophy is consistent with the presence of apoptotic cells in the hair follicle at 5 days after irradiation (Supplementary Fig. S3). Collectively, findings align with RNA-seq-revealed upregulation of apoptosis, keratinocyte differentiation, and keratinization by S-PRT (see **Fig. 1C**) because many of the detected keratins are genes associated with the hair follicle and thus would be involved in its regeneration after damage.

F-PRT ameliorates skin inflammation, even for high radiation dose

Inflammation is characteristic of radiation-induced damage and an important component of wound repair. It is associated with the activation of myeloid cells, such as neutrophils, accompanied by erythema and edema that can manifest in epidermal hyperplasia during the healing process (27). By *in vivo* imaging, F-PRT versus S-PRT activation of myeloid cells was studied through a luminol-based chemiluminescent assay for myeloperoxidase. In mice treated with 30 Gy to their hind limb, less myeloid cell activation occurred after F-PRT versus S-PRT by day 18 ($P = 0.039$) and 27 ($P = 0.064$; **Fig. 3A** and **B**). Thus, F-PRT mitigated inflammatory response to PRT. Moreover, histopathologic analyses (**Fig. 3C** and **D**) showed F-PRT significantly

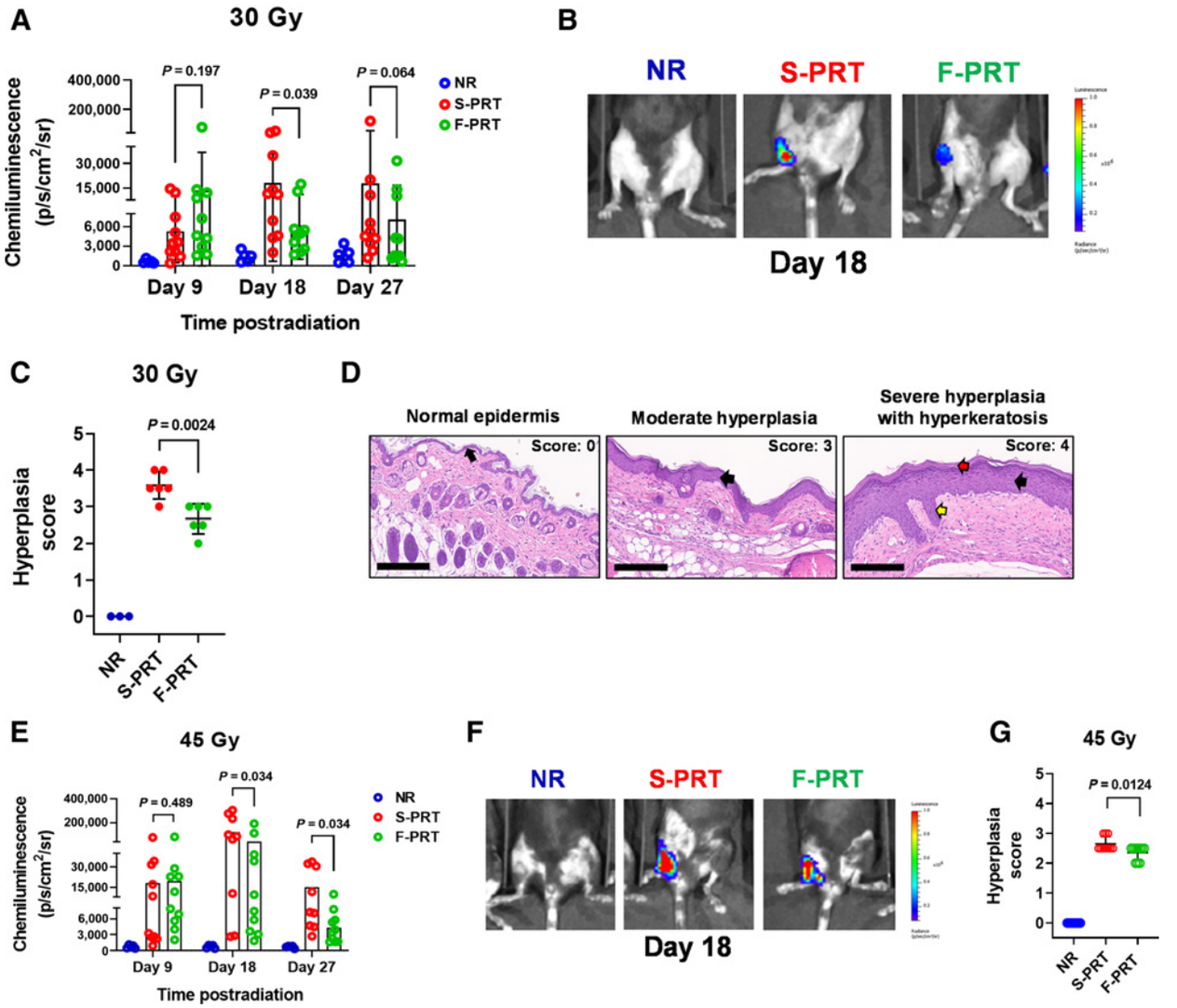

Figure 3.

F-PRT reduces inflammation in the irradiated leg compared with S-PRT. **A** and **B,** For 30 Gy of proton irradiation, quantification of luminol chemiluminescence as a reporter of inflammation (**A**), accompanied by representative images of inflammatory signal at Day 18 (NR, $n = 5$; F-PRT and S-PRT, $n = 10$; statistical analysis by mixed-effects model; **B**). **C,** Blinded histopathologic evaluation of hyperplasia at 27 days post-PRT (NR, $n = 3$; F-PRT and S-PRT, $n = 6$; statistical analysis by Welch t test). **D,** Representative hematoxylin and eosin–stained images of skin hyperplasia. Left, normal epidermal layer (black arrow); middle, moderate chronic damage including a thickened hyperplastic epidermis (black arrow); right, severe chronic damage, including a severely thickened and hyperplastic epidermis (black arrow) with thick layers of orthokeratotic keratin (red arrow) and long rete pegs (yellow arrow). Hematoxylin and eosin, magnification, ×200. Scale bar, 200 μm. **E** and **F,** For 45 Gy of proton irradiation, quantification of luminol chemiluminescence (**E**), accompanied by representative images of inflammatory signal at Day 18 (NR, $n = 5$; F-PRT and S-PRT, $n = 10$; statistical analysis by mixed-effects model; **F**). **G,** Blinded histopathologic evaluation of hyperplasia at 27 days post-PRT. $N = 10$ per group with statistical analysis by Welch t test.

reduced epidermal hyperplasia relative to S-PRT ($P = 0.0024$). These data suggest that F-PRT favorably alters the pathology of wound healing compared with S-PRT.

Next, to define dose dependencies of FLASH RT effect on skin, we considered a dose of 45 Gy. At this higher dose, F-PRT did not lessen the mean skin damage score as both S-PRT and F-PRT led to maximal (score 3.5) damage in several animals (Supplementary Fig. S4). However, similar to that observed at 30 Gy, F-PRT at 45 Gy reduced the extent of myeloid cell activation (**Fig. 3E** and **F**) and epidermal hyperplasia (**Fig. 3G**) compared with S-PRT. Luminol chemiluminescence was significantly less at both day 18 ($P = 0.034$) and day 27 ($P = 0.034$) after 45 Gy of F-PRT compared with the same dose of S-PRT. In concert with FLASH mitigation of inflammation, **Fig. 3G** demonstrates significantly less epidermal hyperplasia ($P = 0.0124$) after 45 Gy of F-PRT compared with S-PRT.

We further investigated if 45 Gy of F-PRT could alter the development of lymphedema as a long-term consequence of high-dose S-PRT. At high dose, lymphedema, and its associated swelling, constitute a major RT-induced toxicity, one that is linked to chronic inflammation (28). Compared with S-PRT, F-PRT did not alter the incidence of lymphedema or its time course (**Fig. 4A**). Lymphedema developed in nearly 40% to 50% of animals after both F-PRT and

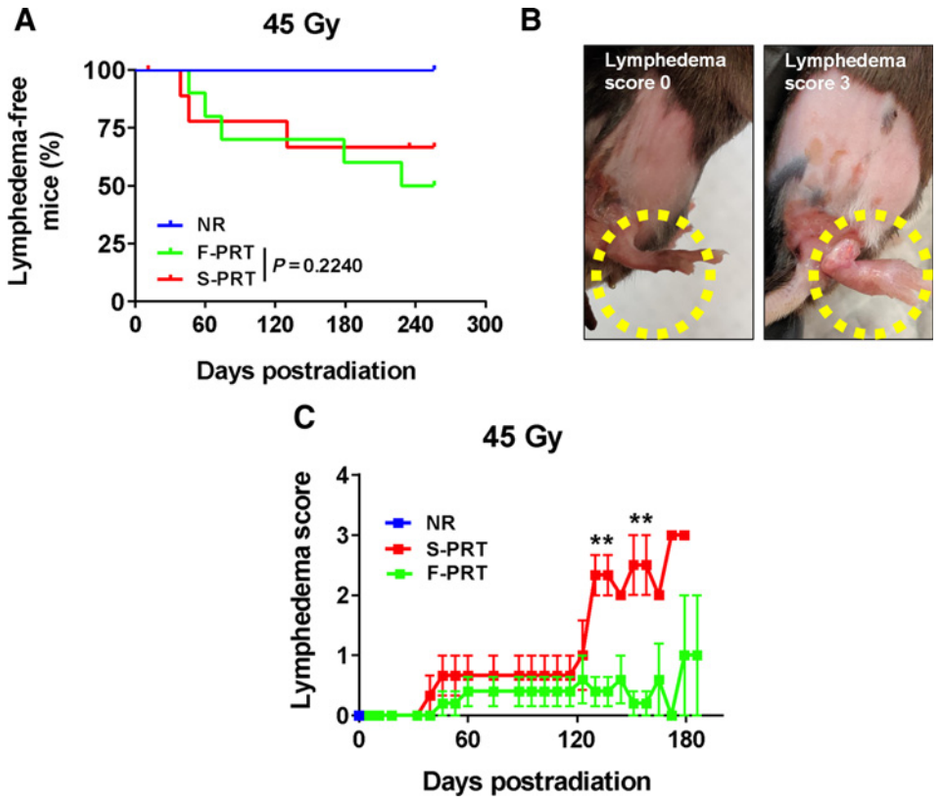

Figure 4.
F-PRT reduces the severity of lymphedema. **A,** Kaplan–Meier curve of lymphedema incidence in mice that received PRT to the hind leg (45 Gy). NR, $n = 5$; F-PRT and S-PRT, $n = 10$; statistical analysis by log-rank test. **B,** Pictures of lymphedema representing scores of 0 (swelling < 1 mm) and 3 (swelling = 3 mm); swelling ≥3 mm mandates euthanasia of the mouse. **C,** Time course of severity among mice that developed lymphedema. F-PRT, $n = 4$; S-PRT, $n = 3$; statistical analysis by multiple cross-sectional t tests with FDR of 0.05; values represent mean ± SEM. **, $P < 0.01$.

S-PRT, and the time of onset was similar. What distinguished F-PRT, however, was the reduced severity of the lymphedemic reaction (**Fig. 4B** and **C**). Scored as a measure of foot thickness, lymphedema was significantly more severe after S-PRT than F-PRT at times of peak response. Collectively, from the above data we glean that at high PRT dose, FLASH may not effectively mitigate acute cellular damage, manifested as skin ulceration; nevertheless, even at higher doses, F-PRT controls the development of inflammation and its consequences.

F-PRT reduces muscle and bone damage relative to S-PRT

We next considered F-PRT effect on mesenchymal tissues of muscle and bone. In histologic sections of F-PRT versus S-PRT-treated (30 Gy) murine leg, F-PRT significantly ($P = 0.0089$) decreased the extent of muscle atrophy compared with S-PRT (**Fig. 5A** and **B**); S-PRT-treated tissue exhibited muscle fibers of smaller cross-sectional diameter that were accompanied by cytoplasmic vacuolation and internalization of nuclei. Similarly, when compared with F-PRT, bones treated with S-PRT showed more evidence of damage that included bone resorption and accompanying pockets of activated osteoclasts and osteoblasts ($P = 0.0065$; **Fig. 5C** and **D**). RNA-seq was performed on bone from F-PRT versus S-PRT mice, revealing several pathways induced by S-PRT but unaltered by F-PRT, corroborating histopathologic findings (**Fig. 5E**, with the involved genes in Supplementary Table S2; also see Supplementary Figs. S5A–S5C for alternative activation states). Pathways such as notochord development and joint development were upregulated by S-PRT, but not by F-PRT. Moreover, pathways related to bone remodeling such as osteoclast differentiation, endochondral bone morphogenesis, and chondrocyte development, were all upregulated by S-PRT, but unaffected by F-PRT. Thus, histologic evidence of reduced (ameliorated) bone damage after F-PRT compared with S-PRT-associated damage alongside evidence of bone remodeling at histological and genetic levels, suggests S-PRT imparted more damage on bone than F-PRT.

F-PRT is equipotent to S-PRT in controlling tumor growth

To be clinically impactful in oncology, F-PRT must not only spare normal tissues, but also provide antitumor efficacy equivalent to standard RT regimens. F-PRT sparing of mesenchymal tissues could be significant to numerous tumor types and anatomical sites, including soft tissue sarcomas. We evaluated the antitumor efficacy of F-PRT compared with S-PRT in two murine models of sarcoma. A sarcoma cell line established from GEMM model *LSL-Kras*$^{G12D/wt}$;*p53*$^{FL/FL}$ (KP) was propagated subcutaneously in the thigh of C57BL/6 mice, and resulting tumors were treated with F-PRT or S-PRT. Tumor response was indistinguishable between the dose rates, both in terms of the regrowth delay (**Fig. 6A**) and the probability of tumor control (**Fig. 6B**). Further evidence of the equivalent antitumor efficacy of F-PRT and S-PRT was found for fibrosarcoma (RIF) tumors propagated in C3H mice. The antitumor efficacy of F-PRT and S-PRT were indistinguishable in both subcutaneous (**Fig. 6C**) and intramuscular orthotopic RIF tumors (**Fig. 6D**), which importantly demonstrates F-PRT to be equivalent to S-PRT in providing tumor control over a range of conditions that could differ between these models such as their levels of oxygenation (29–31).

F-PRT induces less TGFβ1 compared with S-PRT in both murine and canine skin

Finally, we evaluated TGFβ1, which is associated with dose rate-dependent RT effect on normal tissue and a key agent of RT-induced inflammatory reactions (1, 32). TGFβ1 expression was studied by

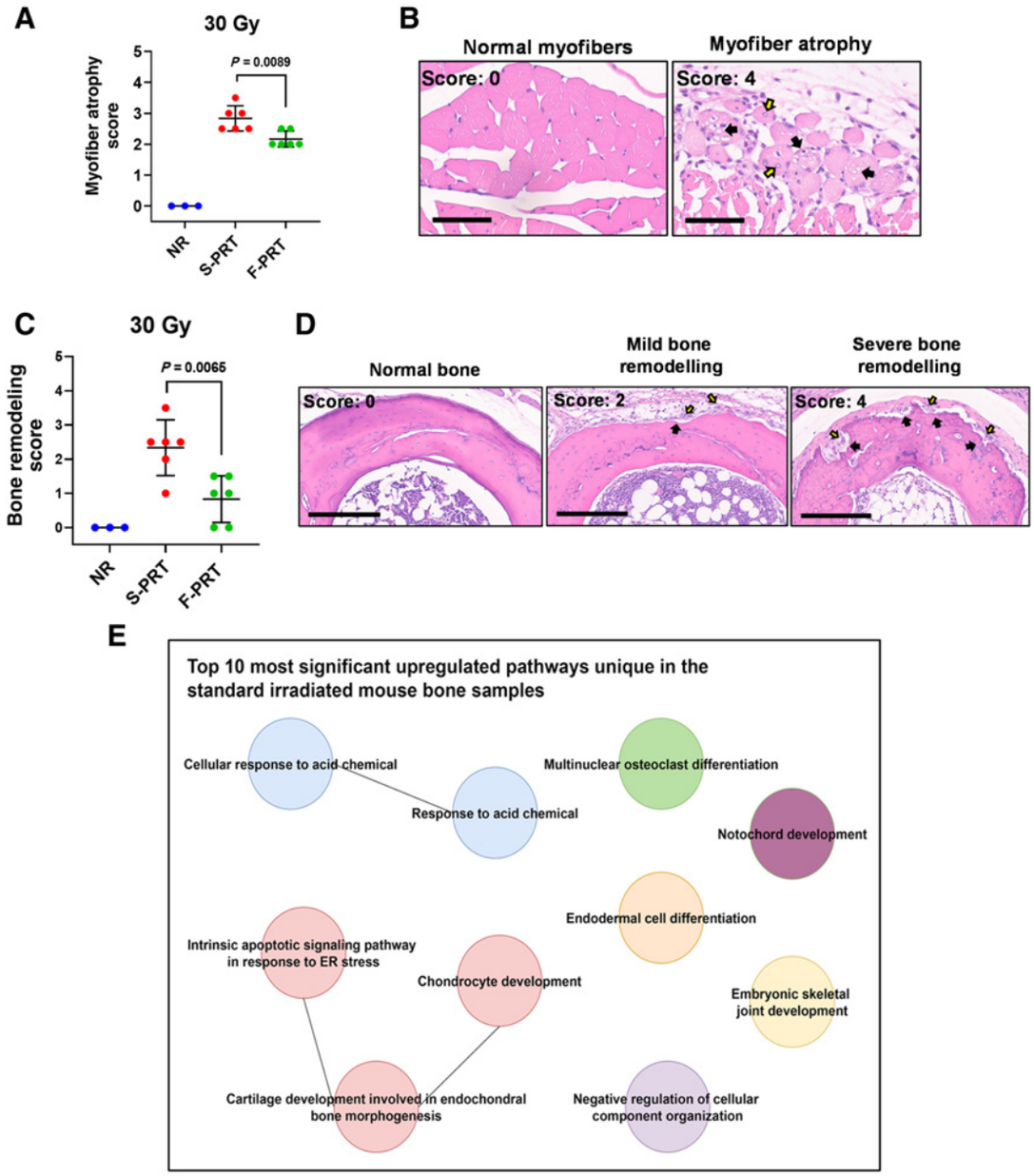

Figure 5.

Damage to the muscle and bone by proton RT is ameliorated by F-PRT as compared with S-PRT. **A,** Blinded evaluation of myofiber atrophy of the gastrocnemius muscle of mice treated by 30 Gy of F-PRT versus S-PRT, at 27 days after RT. Statistical analysis by Welch *t* test. **B,** Representative images of hematoxylin and eosin–stained nonirradiated normal myofibers and myofiber atrophy of irradiated tissue. Myofibers of the irradiated tissue show degenerative changes including decreased cross-sectional diameter (i.e., atrophy), vacuolation of the cytoplasm (black arrows), and internalization of nuclei (yellow arrows). Hematoxylin and eosin, magnification, ×400. Scale bar, 60 μm. **C,** Blinded evaluation of bone remodeling in mice treated by 30 Gy of F-PRT versus S-PRT, at 27 days after PRT. Statistical analysis by Welch *t* test. **D,** Representative images of hematioxylin and eosin–stained bone sections. Left, normal (nonirradiated) bone with normal bone marrow; middle, irradiated bone with resorption (black arrows) lined by activated osteoclasts and osteoblasts (yellow arrows); right, multiple large regions of bone resorption (black arrows) with numerous activated osteoclasts and osteoblasts (yellow arrows). Hematoxylin and eosin, magnification, ×200. Scale bar, 200 μm. For **A** and **C**, NR, $n = 3$; F-PRT and S-PRT, $n = 6$; statistical analysis by Welch *t* test. Values in **A** and **C** represent mean ± SD. **E,** Gene ontology enrichment analysis of the differentially expressed (upregulated) genes in the S-PRT-treated mouse leg bone; $n = 4$ per group.

immunofluorescence in sections of murine skin treated as controls or with F-PRT versus S-PRT (**Fig. 7A**; Supplementary Figs. S6A and S6B). Diffuse epidermal staining of TGFβ1 was noted at 18 days after skin exposure to S-PRT (30 Gy), aligning with inflammation at this time-point (see **Fig. 3A** and **B**). S-PRT significantly ($P < 0.0001$) increased TGFβ1 relative to unirradiated tissue; in contrast, for F-PRT, increases were smaller and statistically indistinguishable from unirradiated tissue ($P = 0.3041$; **Fig. 7B**). Overall, levels of TGFβ1 were higher

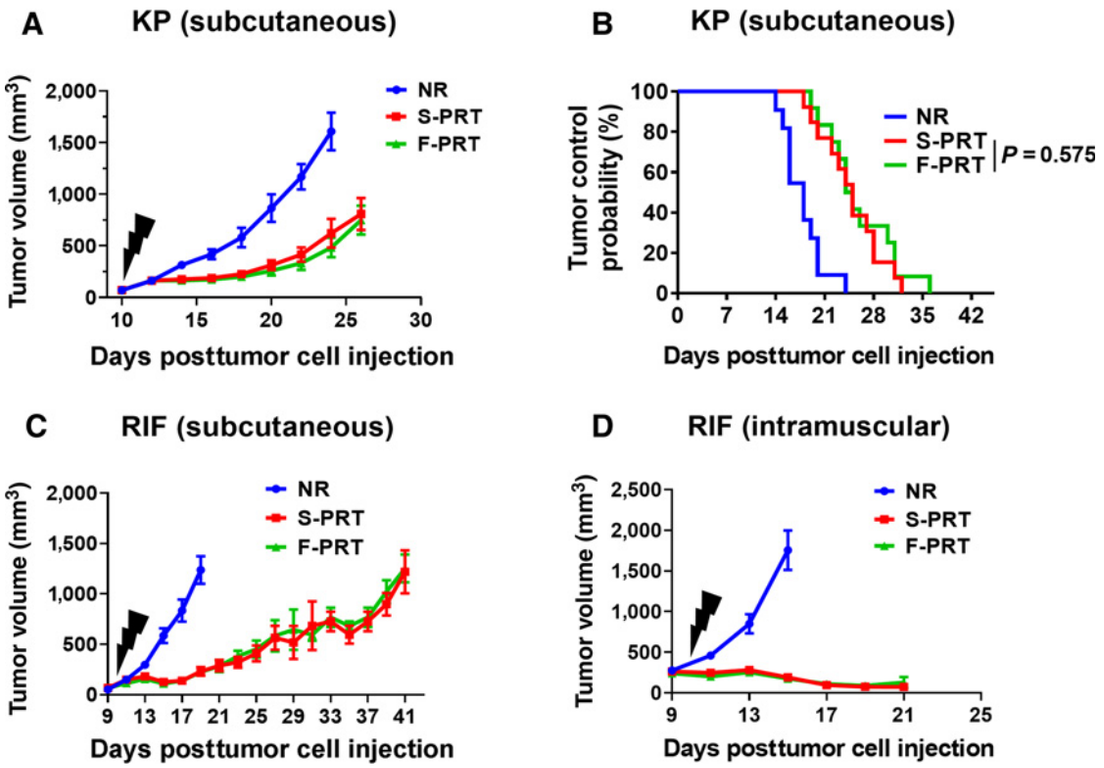

Figure 6.

F-PRT and S-PRT are equipotent in treatment of two models of murine sarcoma. **A,** Growth curve of murine sarcoma established from sarcoma cells isolated from GEMM model LSL-KrasG12D/wt;p53$^{FL/FL}$ and subcutaneously propagated in C67BL/6 mice, followed by irradiation with 12 Gy of F-PRT or S-PRT. $N = 9$, statistical analysis by log-rank test. **B,** Tumor control probability following F-PRT vs. S-PRT of the sarcoma-bearing mice with tumors reaching a volume of <500 mm^3. $N = 13$, statistical analysis by log-rank test. **C,** Growth curve of RIF murine fibrosarcomas subcutaneously propagated in C3H/HeJ mice irradiated with 30 Gy of F-PRT or S-PRT. $N = 8$ mice per group; statistical analysis by log-rank test. **D,** Growth curve of RIF tumor propagated orthotopically in the leg muscle (intramuscular) and irradiated with 30 Gy of F-PRT or S-PRT. $N = 5$ mice per group; statistical analysis by log-rank test. All tumors were irradiated on Day 10 after tumor cell inoculation (black lightning symbol). Data of **A**, **C**, and **D** plot mean ± SD.

after treatment with S-PRT than F-PRT ($P < 0.0001$). ELISAs for TGFβ1 produced similar results (**Fig. 7C**), with S-PRT elevating TGFβ1 compared with unirradiated controls ($P = 0.0023$) whereas cytokine levels after F-PRT were similar to controls ($P = 0.3392$).

Parallel to murine studies, we evaluated TGFβ1 in canine tissues collected as part of an ongoing canine clinical trial on the comparative safety of F-PRT versus S-PRT delivered to the extremities of patient animals with osteosarcoma. Patient characteristics among the dogs on this trial are described in **Table 1**. F-PRT or S-PRT at either 8 or 12 Gy was delivered to tumor and normal tissue of the canine leg, followed in 5 days by standard-of-care limb amputation and sample collection. Irradiated (either F-PRT or S-PRT) and unirradiated normal tissue was collected from each dog. The ratio of TGFβ1 (via ELISA) in irradiated versus unirradiated tissue of the same animal was determined. For the 8 Gy dose, TGFβ1 levels in the irradiated tissue generally differed by no more than 32% compared with the unirradiated tissue; the exception was one subject in the S-PRT group that had over a two-fold elevation. For the 12 Gy dose, differences in TGFβ1 expression were generally more pronounced, and statistically significant for the S-PRT ($P = 0.0494$) animals but not for the F-PRT group ($P = 0.1293$; **Fig. 7D**). At the 12 Gy dose, we further evaluated TGFβ1 by IHC staining in the canine skin (**Fig. 7E** and **F**; Supplementary Figs. S7A and S7B). S-PRT resulted in strong increases in TGFβ1 that were especially noticeable in the hyperplastic epidermis. Staining levels in the irradiated skin of each dog were compared with unirradiated skin from the same animal and showed that S-PRT ($P = 0.047$), but not F-PRT ($P = 0.378$), elevated TGFβ1 protein.

Discussion

In these studies, we have focused on the effects of F-PRT on both epithelial and mesenchymal tissues—specifically soft tissues, bone, and muscle, and found that, compared with S-PRT, F-PRT can reduce skin damage and stem cell depletion; inflammation; late histopathologic changes (myofiber atrophy, bone resorption, hair follicle atrophy, epidermal hyperplasia); and lymphedema. Moreover, we found F-PRT has similar antitumor efficacy against sarcomas using two different models—tumors grown from sarcoma cells isolated from GEMM (*LSL-Kras*$^{G12D/wt}$;*p53*$^{FL/FL}$) mice and tumors grown from the established RIF murine sarcoma line. This is consistent with what we (5) and others have reported using other tumor models (1, 2, 5, 33). Given these findings, our studies offer strong preclinical rationale to evaluate FLASH-PRT in clinical situations where lymphedema and the integrity and/or development of the bone and muscle may be important issues, for example sarcomas, breast cancer, head and neck cancer, and pediatric malignancies. Although we studied single fractions in mice with doses up to 30 to 45 Gy, we do not think these specific doses would be used in patients. More likely, FLASH RT would be used in hypofractionated regimens, perhaps in as few as three to five fractions,

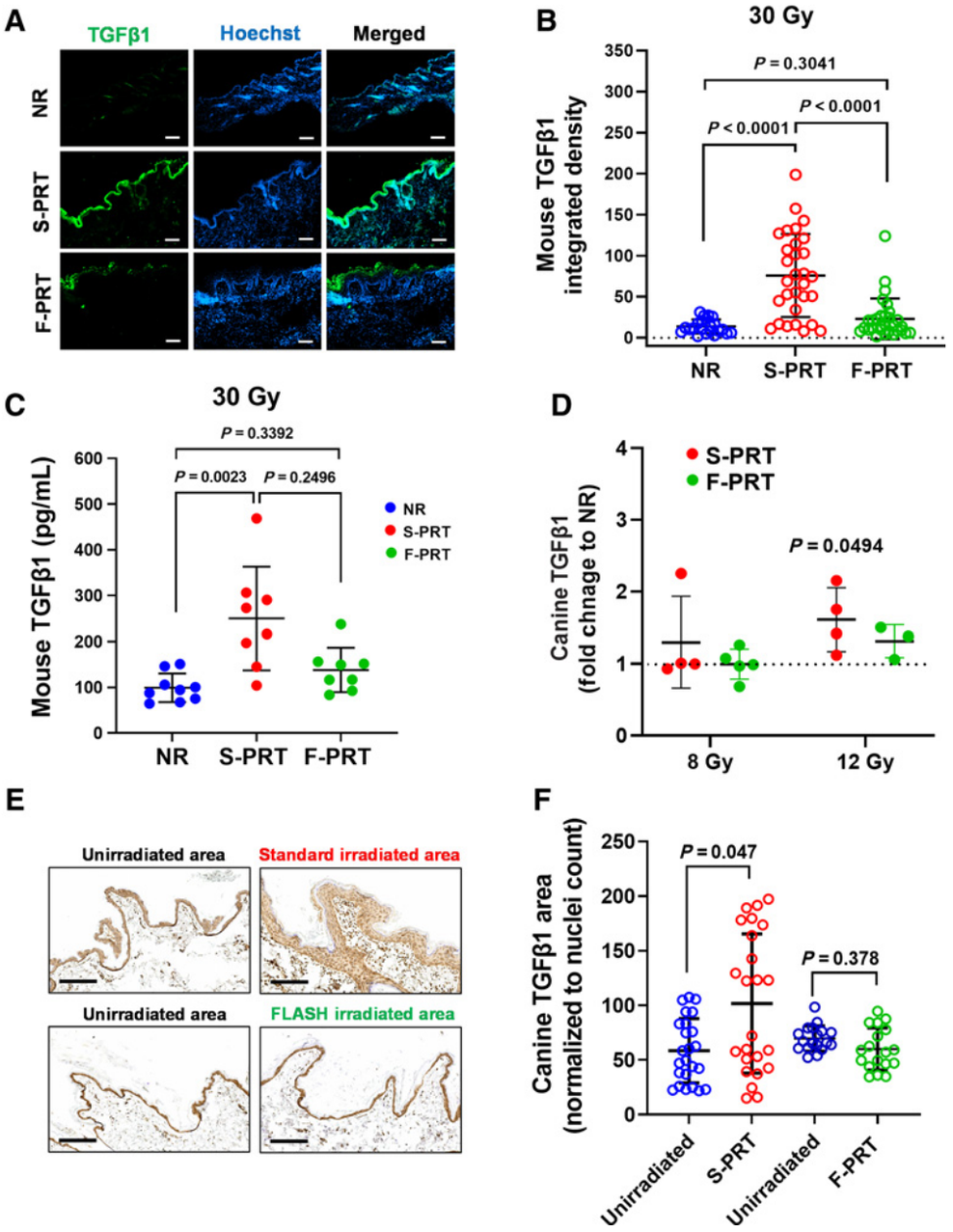

Figure 7.

Lower levels of TGFβ1 are induced in F-PRT-treated mouse and canine skin compared with S-PRT. **A,** Immunofluorescent evaluation of TGFβ1 in mouse skin irradiated with F-PRT or S-PRT (30 Gy; scale bar, 100μm; magnification, ×10). **B,** Quantification of TGFβ1 signal in skin; $n = 5$, with six sections per mouse; statistical analysis by Kruskal–Wallis test. **C,** ELISA of TGFβ1 in the skin of NR ($n = 9$), F-PRT ($n = 8$), and S-PRT ($n = 8$)-treated mice at 18 days post-PRT (30 Gy); statistical analysis by Kruskal–Wallis test. **D,** ELISA of TGFβ1 in the skin of canine patients at 5 days post-PRT; values normalized to NR samples from the same animal; 8 Gy, $n = 5$ (F-PRT) and $n = 4$ (S-PRT); 12 Gy, $n = 3$ (F-PRT) and $n = 4$ (S-PRT). Statistical analysis by paired t test (NR vs. PRT by dog) on the log-transformed data. 8 Gy S-PRT, $P = 0.4364$; 8 Gy F-PRT, $P = 0.8241$; 12 Gy F-PRT, $P = 0.1293$. **E,** IHC evaluation of TGFβ1 in canine skin irradiated with F-PRT or S-PRT (12 Gy) compared with the matched unirradiated area. Scale bar, 200 μm; magnification, ×10. **F,** Quantification of TGFβ1 signal in canine skin; F-PRT, $n = 3$; S-PRT, $n = 4$, with six sections per dog; statistical analysis by mixed effects models. Values represent mean ± SD.

such as those increasingly common for many malignancies including lung and prostate cancers (34). It was beyond the scope of this study to test these hypofractionated regimens, but this is something that we plan to do in the future, both in our mouse models and in a canine trial.

Our studies are novel because we (i) incorporate the investigation of injuries to mesenchymal normal tissues that have been poorly studied to date, including bone; (ii) uniquely apply RNA-seq technology to elucidate differences between FLASH and standard proton RT at the

Table 1. Characteristics of canine patients and treatment parameters for FLASH or standard proton radiotherapy.

Patient ID	Breed	Age (years)	Sex	Weight (kg)	Dose rate (Gy/s)	Dose (Gy)	FLASH or standard
1	Black Lab	11.0	F	33.1	76.2	8.1	F
2[a]	St Bernard	4.5	M	61.4	61.0	4.0	F
3	Mastiff	6.0	F	57.0	103.0	8.1	F
4	Mastiff	6.5	M	59.6	0.5	8.0	S
5	Rottweiler	8.0	M	55.2	111.5	8.0	F
6	Mixed Breed	8.0	M	25.2	0.5	8.1	S
7	Doberman/Great Dane Mix	5.5	F	45.9	0.5	8.1	S
8	Mixed Breed	7.0	M	29.8	111.5[b]	7.6	F
9	Golden Retriever	9.0	M	40.2	114.8[b]	8.0	F
10	Shepherd Mix	9.0	M	35.7	0.5[b]	8.0	S
11	Great Pyrenees	9.0	M	42.9	101.9	12.1	F
12	American Bulldog	10.0	M	45.4	0.5	12.0	S
13[a]	Mixed Breed	8.0	F	36.0	0.1[c]	12.0	S
14[a]	Doberman	8.0	M	36.5	95.5	12.0	F
15	Labradoodle Mix	10.0	M	42.5	122.3	11.9	F
16	Great Dane	5.0	F	71.0	0.5	12.0	S
17	Rottweiler	6.0	F	34.4	0.5	11.9	S
18	Rottweiler/Husky	10.0	M	46.3	128.2	12.0	F
19	Greyhound	1.5	M	28.0	0.6	11.9	S

[a]TGFβ not assayed in these animals.
[b]Irradiated with spread out Bragg peak (SOBP) protons.
[c]Irradiated with photons. See Materials and Methods for complete details.

level of the transcriptome; (iii) include the first ever molecular findings of FLASH effect in canines; and (iv) demonstrate the therapeutic equivalency of FLASH and standard proton therapy in sarcoma tumor models, which are previously uninvestigated yet highly relevant as a disease requiring high-dose radiotherapy. We focus on proton RT (5) because we believe that this modality has the greatest likelihood of being translated widely into human clinical trials in the near future, with a feasibility study recently initiated by Cincinnati Children's and University of Cincinnati Medical Center (35). Current clinical electron energies cannot penetrate deeply enough to treat most common cancers. Likewise, units that can deliver X-rays at FLASH dose rates to treat human cancer are likely years away. In contrast, current-day proton machines can be engineered to treat dogs and even some tumors in human patients at FLASH dose rates. In this study, we have primarily used higher energy "plateau" or early SOBP protons that have a relatively low LET. Further investigations are ongoing on the effect of LET on the FLASH-mediated tumor:normal tissue differential response and will be critical in determining whether the spatial advantages of proton RT will be optimally exploited in F-PRT.

Literature on FLASH protons *in vivo* is very limited, with some conflicting results. One group showed no significant differences between zebrafish given FLASH protons RT (100 Gy/second) versus standard proton RT in most parameters including embryonic survival and spinal curvature (36). In contrast, we have shown and others confirmed that abdominal radiation of mice with FLASH protons RT leads to less toxicity than standard dose rate (4, 5). Yet, it remains important to investigate FLASH protons in sites other than the abdomen. Reassuringly, a very recent report shows FLASH protons to clinically alter skin damage and leg contracture in mouse (19). We similarly note FLASH sparing of clinical skin damage in the current report, but in studies that delve into its underlying cause we further provide the first RNA-seq data on response to FLASH protons (vs. S-PRT). Our studies provide first of its kind data on FLASH sparing of bone, accompanied by corroborating histopathology that informs skin and bone responses to F-PRT versus S-PRT. Although TGFβ1 has been investigated in the context of FLASH RT(19), we uniquely report on its levels in the normal skin of canine patients treated with F-PRT versus S-PRT in studies that importantly demonstrate clinical translation of FLASH molecular endpoints.

Compared with S-PRT, F-PRT reduces severe morbidity that would require euthanasia (**Fig. 1A** and **B**). Limb injury may involve many compartments, but skin damage was a major driver of morbidity in this setting. Skin toxicity after 30 Gy RT was manifested acutely by erythema and dry/moist desquamation and in severe cases, partial/complete skin breakdown with loss of limb function (**Fig. 2A** and **B**); evidence of complete epidermal breakdown (score 3.5) was only seen in the S-PRT arm. F-PRT also reduced the extent of epidermal necrosis (**Fig. 2D** and **E**) and spared hair follicles (**Fig. 2F** and **G**). Sparing of skin toxicity with FLASH electron RT has been reported in mini-pigs (28–34 Gy) and in cat patients (25–41 Gy; ref. 37), and during revisions of this manuscript the feasibility and safety of FLASH electrons in canine patients has also been demonstrated (38). FLASH electrons result in a lower incidence and severity of skin ulceration in mice (39), and FLASH protons reduced skin toxicity and leg contracture (19).

We employed RNA-seq and immunofluorescence of tissue sections to assess underlying mechanisms for the differential effects of FLASH relative to standard dose rate. Pathways related to apoptosis were upregulated with S-PRT but not F-PRT at 5 days postradiation (30 Gy) in murine skin. By immunofluorescence, S-PRT led to greater $Lgr6^+$ cell depletion than F-PRT (**Fig. 2C**; Supplementary Fig. S2). Taken together, our RNA-seq and immunofluorescence data suggest that F-PRT may lead to less severe injury through reduced apoptosis and reduced depletion of skin stem cells, allowing for greater epidermal regeneration in comparison to S-PRT. RNA-seq also showed an upregulation in keratin-related pathways/genes with S-PRT (**Fig. 1C**), which is consistent with the epidermal hyperplasia and hyperkeratosis after S-PRT versus F-PRT (**Fig. 3C** and **D**). Conversely, F-PRT, but not S-PRT, upregulated pathways related to tissue and vascular repair in the skin, including anatomical structural morphogenesis, blood vessel morphogenesis, and vascular development. Hence, this suggests that F-PRT

sparing of skin is through both a reduction in radiation-induced damage and stronger expression of mechanisms for tissue repair.

In addition to studies of epithelial damage in the form of skin injury, we also examined injury to mesenchymal structures. By histopathology, F-PRT (30 Gy) led to less long-term muscle atrophy than S-PRT (**Fig. 5A** and **B**). F-PRT also produced less damage to the bone with less bone resorption and accompanying pockets of activated osteoclasts and osteoblasts, resulting in less bone remodeling (**Fig. 5C** and **D**). This is in keeping with our RNA-seq data that showed S-PRT upregulation of pathways related to bone/chondrocyte development/morphogenesis (**Fig. 5E**). F-PRT also had a sparing effect on lymphedema; in mice that developed lymphedema after 45 Gy, the severity was significantly less with F-PRT than S-PRT (**Fig. 4**).

In all, the sparing effects of F-PRT included both acute and late toxicities that were induced by S-PRT. In the simplest terms, the acute phase of radiation toxicity involves cell death and inflammatory changes to normal tissues that may resolve, whereas late radiation effects involve chronic, unresolved inflammation, microenvironmental changes, and fibrosis that lead to overall organ dysfunction. F-PRT sparing of both acute and late toxicities to skin, bone, and soft tissues was mirrored by changes in inflammatory markers. Luminol chemiluminescence of myeloperoxidase activity showed that with 45 Gy there was less inflammation after F-PRT than S-PRT (**Fig. 3E**). Similar trends in reducing inflammation were seen with 30 Gy (**Fig. 3A**). Thus, even with a dose as high as 45 Gy, inflammation is reduced after FLASH RT, although it may lose its effect in mitigating more severe damage that would require euthanasia (**Fig. 1B**). This difference in inflammation can account for changes in edema and erythema between F-PRT and S-PRT, but the question remains as to whether it explains the sparing of other late toxicities. The relationship between acute and late toxicities following radiation is a complicated one, but TGFβ1 is thought to be a key mediator of both acute inflammation and late fibrosis. Indeed, previous investigations show less TGFβ1 secretion from cells or tissues following FLASH than standard RT (1, 20). Here, we observed that F-PRT induces less acute TGFβ1 secretion in irradiated murine and canine skin than S-PRT (**Fig. 7**). This could also explain the sparing effects of FLASH on lymphedema since in rodent models, RT has been shown to cause lymphatic vessel leakiness with apoptosis of lymphatic endothelial cells and subsequent fibrosis mediated by TGFβ1 (40, 41).

The sparing effects of F-PRT could perhaps involve stem cells. High-dose RT may produce severe toxicity through destruction of stem cells that would survive lower doses and repopulate normal cells killed by radiation. This has been shown for satellite cells in muscle (42), keratin 15 $(Krt15)^+$ basal cells in the esophageal epithelium (43), and $Lgr5^+$ intestinal crypt stem cells (5). Groups including our own have shown that FLASH irradiation of the GI tract can spare proliferating cells in the crypt, in particular $Lgr5^+$ stem cells (2, 5). Here, we find the $Lgr6^+$ stem cell population in the skin to be spared by F-PRT compared with S-PRT. Reasons for cell sparing by FLASH RT are currently unknown, but it has been hypothesized that the generation of hypoxia during radiotherapy may play a role (17). Although it is a controversial area (44), mathematical modeling suggests that under initial conditions of intermediate O_2 tension, FLASH RT may deplete oxygen to levels that alter radiosensitivity (14, 45). Many stem cell compartments (mesenchymal, neural, hematopoietic) exhibit pO_2 ranging from <1% to 8% to maintain their undifferentiated state (35), leading to the hypothesis that FLASH irradiation may spare these stem cell niches as a consequence of their hypoxia (46). In support of this idea, the hypoxia marker EF5 shows the epidermis to be modestly hypoxic and hair follicles moderately-to-severely hypoxic (47). Thus, the hair follicles could be more resistant to killing by FLASH-PRT as a result of a FLASH-mediated decrease in the pO_2 of their microenvironment. As hair follicles serve as one source of $Lgr6^+$ cells (48), $Lgr6^+$ cell sparing by FLASH also aligns with its sparing of hair follicles.

In addition to the above-studied mechanisms, our RNA-seq analyses provide a wealth of novel data to continue to be explored for its revelations about FLASH mechanism. For example, RNA-seq of bones reveals F-PRT, but not S-PRT, is associated with the upregulation of an integrated cluster of immune pathways. Among these, the activation of innate immune response, as well as response to type 1 IFN could potentially alter healing (49) and/or tumor response (50) to F-PRT compared with S-PRT and could serve to inform new avenues of investigation.

In summary, we demonstrate FLASH-proton RT to spare murine skin, muscle, and bone compared with standard-proton RT. F-PRT minimally changes TGFβ1 levels in the skin of both mice and dogs while RNA-seq data and IHC, immunofluorescence, and pathologic assays suggest FLASH protons to decrease radiation damage and favor mechanisms of tissue repair. The equipotent effect of FLASH- and standard-proton RT in controlling sarcoma growth are demonstrated here for the first time and, together with the above findings, support further investigation of FLASH RT toward clinical applications that would benefit from its sparing effects on skin and mesenchymal tissues.

Authors' Disclosures

G. Skoufos reports other support from State Scholarships Foundation (IKY) - Greece during the conduct of the study. M. Putt reports grants from NIH during the conduct of the study. J. Metz reports personal fees from Varian and IBA outside the submitted work. C. Koumenis reports personal fees from IBA, nonfinancial support from Varian, and personal fees from Mayo Clinic outside the submitted work. K.A. Cengel reports other support from Simphotek outside the submitted work; also has a patent for US9999779B2 issued and a patent for US20190099491A1 pending. A. Maity reports grants from Merck outside the submitted work. T.M. Busch reports other support from Simphotek and personal fees from Lumeda outside the submitted work. No disclosures were reported by the other authors.

Authors' Contributions

A. Velalopoulou: Conceptualization, data curation, formal analysis, investigation, visualization, writing–original draft, writing–review and editing. **I.V. Karagounis:** Conceptualization, data curation, formal analysis, investigation, visualization, writing–original draft, writing–review and editing. **G.M. Cramer:** Conceptualization, data curation, formal analysis, investigation, visualization, writing–original draft, writing–review and editing. **M.M. Kim:** Validation, investigation, methodology, writing–review and editing. **G. Skoufos:** Data curation, formal analysis, visualization, writing–review and editing. **D. Goia:** Investigation, writing–review and editing. **S. Hagan:** Investigation, visualization, writing–review and editing. **I.I. Verginadis:** Investigation, visualization, writing–review and editing. **K. Shoniyozov:** Validation, investigation, methodology, writing–review and editing. **J. Chiango:** Investigation, writing–review and editing. **M. Cerullo:** Investigation, writing–review and editing. **K. Varner:** Investigation, writing–review and editing. **L. Yao:** Investigation, visualization, writing–review and editing. **L. Qin:** Supervision, investigation, visualization, writing–review and editing. **A.G. Hatzigeorgiou:** Supervision, validation, writing–review and editing. **A.J. Minn:** Conceptualization, writing–review and editing. **M. Putt:** Formal analysis, writing–review and editing. **M. Lanza:** Investigation, visualization, writing–review and editing. **C.-A. Assenmacher:** Investigation, visualization, writing–review and editing. **E. Radaelli:** Supervision, validation, investigation, visualization, writing–review and editing. **J. Huck:** Supervision, investigation, writing–review and editing. **E. Diffenderfer:** Validation, investigation, methodology, writing–review and editing. **L. Dong:** Validation, writing–review and editing. **J. Metz:** Conceptualization, funding acquisition, writing–review and editing. **C. Koumenis:** Conceptualization, supervision, funding acquisition, project administration, writing–review and editing. **K.A. Cengel:** Conceptualization, data curation, supervision, funding acquisition, investigation, visualization, methodology,

writing–original draft, project administration, writing–review and editing. **A. Maity:** Conceptualization, supervision, funding acquisition, writing-original draft, project administration, writing–review and editing. **T.M. Busch:** Conceptualization, data curation, formal analysis, supervision, funding acquisition, validation, visualization, writing–original draft, project administration, writing–review and editing.

Acknowledgments

The authors recognize services provided through the Small Animal Imaging Facility and the Cell and Animal Irradiation Core at the University of Pennsylvania. The authors thank Dazheng Zhang for his contribution to initial statistical analyses. The Department of Radiation Oncology and the Translational Center of Excellence (TCE) of the Abramson Cancer Center at UPenn are acknowledged for financial support. Additional funding (for G. Skoufos) was provided (Greece and European Social Fund-ESF) through the Operational Programme "Human Resources Development, Education and Lifelong Learning" in the context of the project "Strengthening Human Resources Research Potential via Doctorate Research" (MIS-5000432), implemented by the State Scholarships Foundation (IKY), in the form of a PhD Scholarship.

Received May 13, 2021; revised June 29, 2021; accepted July 27, 2021; published first July 28, 2021.

References

1. Favaudon V, Caplier L, Monceau V, Pouzoulet F, Sayarath M, Fouillade C, et al. Ultrahigh dose-rate FLASH irradiation increases the differential response between normal and tumor tissue in mice. Sci Transl Med 2014;6:245ra93.
2. Levy K, Natarajan S, Wang J, Chow S, Eggold JT, Loo PE, et al. Abdominal FLASH irradiation reduces radiation-induced gastrointestinal toxicity for the treatment of ovarian cancer in mice. Sci Rep 2020;10:21600.
3. LaRiviere MJ, Santos PMG, Hill-Kayser CE, Metz JM. Proton therapy. Hematol Oncol Clin North Am 2019;33:989–1009.
4. Zhang Q, Cascio E, Li C, Yang Q, Gerweck LE, Huang P, et al. FLASH investigations using protons: design of delivery system, preclinical setup and confirmation of FLASH Effect with protons in animal systems. Radiat Res 2020; 194:656–64.
5. Diffenderfer ES, Verginadis II, Kim MM, Shoniyozov K, Velalopoulou A, Goia D, et al. Design, Implementation, and in Vivo Validation of a Novel Proton FLASH Radiation Therapy System. Int J Radiat Oncol Biol Phys 2020;106:440–8.
6. Tepper JE. Gunderson & Tepper's Clinical Radiation Oncology. Philadelphia, PA: Elsevier, Inc; 2021.
7. Haubner F, Ohmann E, Pohl F, Strutz J, Gassner HG. Wound healing after radiation therapy: review of the literature. Radiat Oncol 2012;7:162.
8. Kwon S, Janssen CF, Velasquez FC, Zhang S, Aldrich MB, Shaitelman SF, et al. Radiation dose-dependent changes in lymphatic remodeling. Int J Radiat Oncol Biol Phys 2019;105:852–60.
9. Cormier JN, Askew RL, Mungovan KS, Xing Y, Ross MI, Armer JM. Lymphedema beyond breast cancer: a systematic review and meta-analysis of cancer-related secondary lymphedema. Cancer 2010;116:5138–49.
10. McLaughlin SA, Brunelle CL, Taghian A. Breast cancer-related lymphedema: risk factors, screening, management, and the impact of locoregional treatment. J Clin Oncol 2020;38:2341–50.
11. Davis AM, O'Sullivan B, Turcotte R, Bell R, Catton C, Chabot P, et al. Late radiation morbidity following randomization to preoperative versus postoperative radiotherapy in extremity soft tissue sarcoma. Radiother Oncol 2005;75: 48–53.
12. Montay-Gruel P, Acharya MM, Petersson K, Alikhani L, Yakkala C, Allen BD, et al. Long-term neurocognitive benefits of FLASH radiotherapy driven by reduced reactive oxygen species. Proc Natl Acad Sci U S A 2019;116: 10943–51.
13. Simmons DA, Lartey FM, Schuler E, Rafat M, King G, Kim A, et al. Reduced cognitive deficits after FLASH irradiation of whole mouse brain are associated with less hippocampal dendritic spine loss and neuroinflammation. Radiother Oncol 2019;139:4–10.
14. Petersson K, Adrian G, Butterworth K, McMahon SJ. A quantitative analysis of the role of oxygen tension in FLASH radiation therapy. Int J Radiat Oncol Biol Phys 2020;107:539–47.
15. Adrian G, Konradsson E, Lempart M, Back S, Ceberg C, Petersson K. The FLASH effect depends on oxygen concentration. Br J Radiol 2020;93:20190702.
16. Kim YE, Gwak SH, Hong BJ, Oh JM, Choi HS, Kim MS, et al. Effects of ultra-high doserate FLASH irradiation on the tumor microenvironment in lewis lung carcinoma: role of myosin light chain. Int J Radiat Oncol Biol Phys 2021;109: 1440–53.
17. Spitz DR, Buettner GR, Petronek MS, St-Aubin JJ, Flynn RT, Waldron TJ, et al. An integrated physico-chemical approach for explaining the differential impact of FLASH versus conventional dose rate irradiation on cancer and normal tissue responses. Radiother Oncol 2019;139:23–7.
18. Fouillade C, Curras-Alonso S, Giuranno L, Quelennec E, Heinrich S, Bonnet-Boissinot S, et al. FLASH irradiation spares lung progenitor cells and limits the incidence of radio-induced senescence. Clin Cancer Res 2020; 26:1497–506.
19. Cunningham S, McCauley S, Vairamani K, Speth J, Girdhani S, Abel E, et al. FLASH proton pencil beam scanning irradiation minimizes radiation-induced leg contracture and skin toxicity in mice. Cancers 2021;13:1012.
20. Buonanno M, Grilj V, Brenner DJ. Biological effects in normal cells exposed to FLASH dose rate protons. Radiother Oncol 2019;139:51–5.
21. Dobin A, Davis CA, Schlesinger F, Drenkow J, Zaleski C, Jha S, et al. STAR: ultrafast universal RNA-seq aligner. Bioinformatics 2013;29:15–21.
22. Li B, Dewey CN. RSEM: accurate transcript quantification from RNA-Seq data with or without a reference genome. BMC Bioinformatics 2011;12:323.
23. Leng N, Dawson JA, Thomson JA, Ruotti V, Rissman AI, Smits BM, et al. EBSeq: an empirical Bayes hierarchical model for inference in RNA-seq experiments. Bioinformatics 2013;29:1035–43.
24. Noda S, Iwakawa M, Ohta T, Iwata M, Yang M, Goto M, et al. Inter-strain variance in late phase of erythematous reaction or leg contracture after local irradiation among three strains of mice. Cancer Detect Prev 2005;29:376–82.
25. Gross S, Gammon ST, Moss BL, Rauch D, Harding J, Heinecke JW, et al. Bioluminescence imaging of myeloperoxidase activity in vivo. Nat Med 2009;15: 455–61.
26. RWt D, Snyder E, Miller J, Carter S, Houser C, Klampatsa A, et al. Luminol chemiluminescence reports photodynamic therapy-generated neutrophil activity in vivo and serves as a biomarker of therapeutic efficacy. Photochem Photobiol 2019;95:430–8.
27. Dombrowsky AC, Schauer J, Sammer M, Blutke A, Walsh DWM, Schwarz B, et al. Acute skin damage and late radiation-induced fibrosis and inflammation in murine ears after high-dose irradiation. Cancers (Basel) 2019;11:727.
28. Ly CL, Kataru RP, Mehrara BJ. Inflammatory manifestations of lymphedema. Int J Mol Sci 2017;18:171.
29. Kavanagh MC, Sun A, Hu Q, Hill RP. Comparing techniques of measuring tumor hypoxia in different murine tumors: Eppendorf pO2 Histograph, [3H]misonidazole binding and paired survival assay. Radiat Res 1996;145:491–500.
30. Horsman MR, Khalil AA, Siemann DW, Grau C, Hill SA, Lynch EM, et al. Relationship between radiobiological hypoxia in tumors and electrode measurements of tumor oxygenation. Int J Radiat Oncol Biol Phys 1994;29:439–42.
31. Sitnik TM, Hampton JA, Henderson BW. Reduction of tumour oxygenation during and after photodynamic therapy in vivo: effects of fluence rate. Br J Cancer 1998;77:1386–94.
32. Franko AJ, Sharplin J, Ghahary A, Barcellos-Hoff MH. Immunohistochemical localization of transforming growth factor beta and tumor necrosis factor alpha in the lungs of fibrosis-prone and "non-fibrosing" mice during the latent period and early phase after irradiation. Radiat Res 1997;147:245–56.
33. Montay-Gruel P, Acharya MM, Goncalves JP, Petit B, Petridis IG, Fuchs P, et al. Hypofractionated FLASH-RT as an effective treatment against glioblastoma that reduces neurocognitive side effects in mice. Clin Cancer Res 2021;27:775–84.
34. Folkert MR, Timmerman RD. Stereotactic ablative body radiosurgery (SABR) or Stereotactic body radiation therapy (SBRT). Adv Drug Deliv Rev 2017;109:3–14.
35. Mohyeldin A, Garzon-Muvdi T, Quinones-Hinojosa A. Oxygen in stem cell biology: a critical component of the stem cell niche. Cell Stem Cell 2010;7:150–61.
36. Beyreuther E, Brand M, Hans S, Hideghety K, Karsch L, Lessmann E, et al. Feasibility of proton FLASH effect tested by zebrafish embryo irradiation. Radiother Oncol 2019;139:46–50.
37. Vozenin MC, De Fornel P, Petersson K, Favaudon V, Jaccard M, Germond JF, et al. The advantage of FLASH radiotherapy confirmed in mini-pig and cat-cancer patients. Clin Cancer Res 2019;25:35–42.
38. Konradsson E, Arendt ML, Bastholm JK, Borresen B, Hansen AE, Back S, et al. Establishment and initial experience of clinical FLASH radiotherapy in canine cancer patients. Front Oncol 2021;11:658004.

39. Soto LA, Casey KM, Wang J, Blaney A, Manjappa R, Breitkreutz D, et al. FLASH irradiation results in reduced severe skin toxicity compared to conventional-dose-rate irradiation. Radiat Res 2020;194:618–24.
40. Narayanan SA, Ford J, Zawieja DC. Impairment of lymphatic endothelial barrier function by X-ray irradiation. Int J Radiat Biol 2019;95:562–70.
41. Avraham T, Yan A, Zampell JC, Daluvoy SV, Haimovitz-Friedman A, Cordeiro AP, et al. Radiation therapy causes loss of dermal lymphatic vessels and interferes with lymphatic function by TGF-beta1-mediated tissue fibrosis. Am J Physiol Cell Physiol 2010;299:C589–605.
42. Collins CA, Olsen I, Zammit PS, Heslop L, Petrie A, Partridge TA, et al. Stem cell function, self-renewal, and behavioral heterogeneity of cells from the adult muscle satellite cell niche. Cell 2005;122:289–301.
43. Giroux V, Lento AA, Islam M, Pitarresi JR, Kharbanda A, Hamilton KE, et al. Long-lived keratin 15+ esophageal progenitor cells contribute to homeostasis and regeneration. J Clin Invest 2017;127:2378–91.
44. Cao X, Zhang R, Esipova TV, Allu SR, Ashraf R, Rahman M, et al. Quantification of oxygen depletion during FLASH irradiation in vitro and in vivo. Int J Radiat Oncol Biol Phys 2021.
45. Pratx G, Kapp DS. A computational model of radiolytic oxygen depletion during FLASH irradiation and its effect on the oxygen enhancement ratio. Phys Med Biol 2019;64:185005.
46. Pratx G, Kapp DS. Ultra-high-dose-rate FLASH irradiation may spare hypoxic stem cell niches in normal tissues. Int J Radiat Oncol Biol Phys 2019;105:190–2.
47. Evans SM, Schrlau AE, Chalian AA, Zhang P, Koch CJ. Oxygen levels in normal and previously irradiated human skin as assessed by EF5 binding. J Invest Dermatol 2006;126:2596–606.
48. Fullgrabe A, Joost S, Are A, Jacob T, Sivan U, Haegebarth A, et al. Dynamics of Lgr6(+) progenitor cells in the hair follicle, sebaceous gland, and interfollicular epidermis. Stem Cell Reports 2015;5:843–55.
49. Conrad C, Gilliet M. Type I IFNs at the interface between cutaneous immunity and epidermal remodeling. J Invest Dermatol 2012;132:1759–62.
50. Wisdom AJ, Mowery YM, Hong CS, Himes JE, Nabet BY, Qin X, et al. Single cell analysis reveals distinct immune landscapes in transplant and primary sarcomas that determine response or resistance to immunotherapy. Nat Commun 2020;11:6410.